The Role of Monsoon-like Zonally Asymmetric Heating in Interhemispheric Transport

Gang Chen[1], Clara Orbe[2,3,4], and Darryn Waugh[3]

[1]Department of Atmospheric and Oceanic Sciences, University of California-Los Angeles, Los Angeles, California, USA.
[2]Global Modeling and Assimilation Office (GMAO), NASA Goddard Space Flight Center, Greenbelt, Maryland, USA.
[3]Department of Earth and Planetary Sciences, Johns Hopkins University, Baltimore, Maryland, USA.
[4]Goddard Earth Sciences Technology and Research (GESTAR), Columbia, Maryland, USA.

Key Points:

- The seasonal cycle of the zonally averaged Hadley cell alone results in slow interhemispheric transport
- Additional monsoon-like heating accelerates interhemispheric transport to more realistic values
- Monsoon-like heating produces an upper-tropospheric cross-equatorial transport pathway

Corresponding author: Gang Chen, gchenpu@ucla.edu

Abstract

While the importance of the seasonal migration of the zonally averaged Hadley circulation on interhemispheric transport of trace gases has been recognized, few studies have examined the role of the zonally asymmetric monsoonal circulation. This study investigates the role of monsoon-like zonally asymmetric heating on interhemispheric transport using a dry atmospheric model that is forced by idealized Newtonian relaxation to a prescribed radiative equilibrium temperature. When only the seasonal cycle of zonally symmetric heating is considered, the mean age of air in the Southern Hemisphere since last contact with the Northern Hemisphere midlatitude boundary layer, is much larger than the observations. The introduction of monsoon-like zonally asymmetric heating not only reduces the mean age of tropospheric air to more realistic values, but also produces an upper-tropospheric cross-equatorial transport pathway in boreal summer that resembles the transport pathway simulated in the NASA Global Modeling Initiative (GMI) Chemistry Transport Model driven with MERRA meteorological fields. These results highlight the monsoon-induced eddy circulation plays an important role in the interhemispheric transport of long-lived chemical constituents.

1 Introduction

Interhemispheric transport is crucial for the global distribution of long-lived trace gases in the troposphere, which are primarily emitted from the Northern Hemisphere (NH) midlatitude surface. Cross-equatorial transport has traditionally been quantified by the time scale inferred from the two-box model with each hemisphere being a box, using measurements of rapidly growing, long-lived chemical species such as chloroflourocarbons (CFCs) and sulfur hexaflouride (SF_6) [e.g., *Heimann and Keeling*, 1986; *Maiss and Levin*, 1994; *Levin and Hesshaimer*, 1996; *Geller et al.*, 1997]. The mechanisms of interhemispheric transport have been interpreted in terms of the seasonal migration of the zonally averaged Hadley circulation [*Bowman and Cohen*, 1997], the strength and position of tropical convection [*Lintner et al.*, 2004], or upper tropospheric westerly ducts associated with Rossby wave breaking [*Staudt et al.*, 2001]. Recently, *Orbe et al.* [2016] identified the Asian monsoon anticyclone as an important transport pathway for cross-equatorial transport in the NASA Global Modeling Initiative (GMI) Chemistry Transport Model driven with MERRA meteorological fields (referred to as the GMI-MERRA model hereafter). This paper will analyze the transport in an idealized atmospheric model in which seasonally-varying zonally symmetric heating and the monsoon-like zonally asymmetric heating can be separated, and thus interhemispheric transport by the seasonally-varying Hadley circulation can be compared with that by the monsoonal circulation. A schematic summary of the two mechanisms is depicted in Fig. 1, with the boreal winter Hadley cell transporting the NH air mass across the equator in the lower level versus the boreal summer monsoon exchanging mass between the two hemispheres in the upper level. Since the mass of each hemisphere does not change in the time mean, the Hadley cell also transports mass back to the NH in the upper troposphere, and the zonally asymmetric monsoon circulation helps maintain the mass balance by either the upper tropospheric two-way eddy mixing or the lower tropospheric branch of the monsoon circulation.

Tracer transport in the global atmosphere can be thought of as the consequence of the diabatic overturning circulation and isentropic mixing [e.g., *Plumb and Mahlman*, 1987; *Bowman and Carrie*, 2002; *Bowman and Erukhimova*, 2004; *Chen and Plumb*, 2014]. In the tropics, the probability distribution functions (PDFs) of column water vapor (CWV) and trace gases of different chemical sources/sinks exhibit similar exponential tails, providing observational evidence of tropical convection's influence on tracer distributions [*Neelin et al.*, 2010; *Lintner et al.*, 2011]. Chemical transport models also show that convection can enhance vertical and horizontal tracer transport [e.g., *Gilliland and Hartley*, 1998; *Hess*, 2005; *Erukhimova and Bowman*, 2006], and that interhemispheric transport is modulated by the seasonal migration of the Hadley circulation [*Bowman and Cohen*, 1997]. Meanwhile, the Asian monsoon anticyclone is associated with horizontal eddy shedding and irreversible
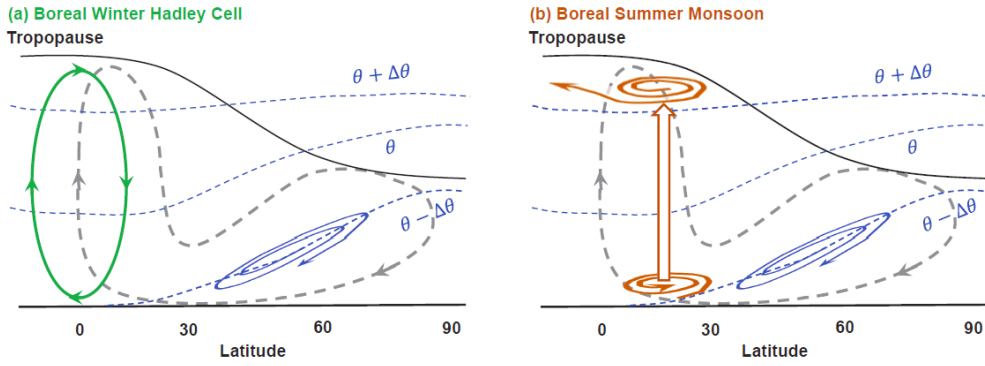
Figure 1. Schematic summary of the two mechanisms of interhemispheric transport: (a) the boreal winter Hadley cell (green) transporting mass across the equator in the lower troposphere, and (b) the boreal summer monsoon (red), characterized by the lower-level convergence and upper-level divergence, that exchanges mass between the two hemispheres through the upper-tropospheric anticyclone. In both (a) and (b), gray dashed lines indicate the annual mean residual meridional circulation, and blue lines depict isentropic surfaces and eddy mixing.

mixing of trace gases along its southward edge [*Popovic and Plumb*, 2001], and upper tropospheric Rossby wave breaking is very efficient at mixing air masses across the equator [*Waugh et al.*, 1994]. Since tropospheric transport displays transport barriers in the subtropics [*Haynes and Shuckburgh*, 2000; *Allen and Nakamura*, 2001; *Chen and Plumb*, 2014], interhemispheric transport is also quantified by means of a three-box model, in which the tropical box is sandwiched between two extratropical boxes [*Bowman and Carrie*, 2002; *Bowman and Erukhimova*, 2004].

While the aforementioned advection-diffusion paradigm as well as the two- and three-box models are important for our understanding of global tracer transport, the spatial pattern of interhemispheric transport is better quantified by the Green function that captures where, and after how long, the air in the Southern Hemisphere (SH) was last in the NH. *Holzer and Boer* [2001] examined the mean transport climate, as defined by the Green function with respect to localized sources in a climate model, and found that interhemispheric exchange times, mixing times, and mean transit times all increase by about 10% under climate warming. The seasonality of the Green function can also help elucidate the transport pathway by which interhemispheric exchange occurs and its relation to both the seasonal movement of the Hadley cell and the monsoon [*Holzer*, 1999]. Furthermore, *Holzer* [2009a,b] developed a rigorous path-density diagnostic that identifies the regions through which air passes from the source region (e.g., NH high latitudes) to the receptor region (e.g., SH high latitudes).

Using surface measurements of SF_6 and CFCs, *Waugh et al.* [2013] and *Holzer and Waugh* [2015] obtained the mean age and the spectral width of the transit time distribution (TTD) for different locations in the troposphere since last contact at the NH midlatitude surface, which *Orbe et al.* [2016] then compared with the results from the GMI-MERRA simulation. They also showed that the TTD in the GMI-MERRA simulation is characterized by distinct fast advective transport and slow diffusive recirculations that are deemed important for tracers of short and long lifetimes, respectively, and that the upper-tropospheric cross-equatorial flow in boreal summer is linked to the Asian summer monsoon.

The paper is outlined as follows. Section 2 introduces the idealized model of the atmosphere and the diagnostic of tracer transport. The responses in the TTD and its characteristics to seasonally-varying zonally symmetric heating and the monsoon-like zonally-asymmetric heating are compared and discussed in section 3. The transport pathway respon-

sible for the simulated TTD is further analyzed in section 4, and the importance of monsoon-induced eddy circulations is highlighted. Finally, section 5 provides a brief summary of the paper.

2 Idealized model and transport diagnostics

2.1 Idealized atmospheric model

We use the Geophysical Fluid Dynamical Laboratory (GFDL) spectral atmospheric dynamical core. The model solves the primitive equations on the sphere with *Held and Suarez* [1994] physics: it is forced by Newtonian relaxation to a prescribed radiative equilibrium temperature and damped by Rayleigh friction in the planetary boundary layer. Readers are referred to *Held and Suarez* [1994] for details of model physics, and the same Held-Suarez parameters are employed here unless otherwise stated.

We introduce additional perturbations to the Held-Suarez equilibrium temperature to mimic the diabatic heating associated with the seasonal cycle in radiative heating and latent heat release, as well as the zonally asymmetric monsoon circulation. More specifically, the radiative equilibrium temperature is specified as

$$T_{eq} = \max\{200, [315 - 20\,\hat{t}\sin\phi - 60\sin^2\phi - 10\log(\frac{p}{10^5})\cos^2\phi](\frac{p}{10^5})^\kappa + T'_{eq}\}, \tag{1}$$

Here ϕ is latitude, p is pressure, $\kappa = R/c_p = 2/7$, where R is the gas constant of dry air and c_p is specific heat of dry air at constant pressure. The term $20\,\hat{t}\sin\phi$ gives the zonally symmetric off-equatorial heating in summer and cooling in winter. The parameter $\hat{t}$ determines the timing throughout the seasonal cycle, which permits to run the model with either perpetual equinoctial or seasonally-varying radiative equilibrium temperature. The perpetual equinoctial condition is mimicked by setting $\hat{t} = 0$. To produce a seasonal cycle from winter to summer, we set $\hat{t} = \cos(\frac{2\pi t}{1\,\text{year}})$, where t denotes time. *Chen and Plumb* [2014] showed that the off-equatorial heating can produce a cross-equatorial Hadley circulation and an associated wintertime subtropical jet, which can in turn suppress the eddy mixing at the jet core and lead to more wave breaking at the jet flanks.

Additionally, T'_{eq} specifies a wavenumber 2 perturbation in the NH subtropics to mimic the zonally asymmetric effect of Asian and North American monsoons [e.g., *Shaw*, 2014].

$$T'_{eq} = \frac{\pi}{2}A_0\mathcal{H}(-\hat{t})\sin(2\lambda)\Phi(\phi, p) \tag{2}$$

Here $\mathcal{H}()$ is a heaviside function. This heaviside function switches on the zonally asymmetric monsoon-like heating in the NH summer but turns it off during the SH summer. The perturbation has an amplitude of $\frac{\pi}{2}A_0$ with a meridional and vertical structure centered at the latitude of $\phi_0 = 5\pi/36 = 25°$ and midtroposphere ($\sim$600 hPa)

$$\Phi(\phi, p) = \begin{cases} \cos^2[6(\phi - \phi_0)]\sin(\pi\frac{10^5 - p}{0.8\times10^5}), & (|\phi - \phi_0| \le \frac{\pi}{12},\ p \ge 0.2\times10^5\text{Pa}) \\ 0, & (\text{elsewhere}) \end{cases} \tag{3}$$

Such a meridional pattern has been used to study the impact of zonally symmetric off-equatorial heating [*Plumb and Hou*, 1992] on the cross-equatorial Hadley cell and the influence of zonally asymmetric heating [*Zhai and Boos*, 2015] on the monsoon circulation. Here $\hat{t} = -1$ represents the July condition with the zonally asymmetric heating centered at 25°N. The perturbation T'_{eq} is approximately confined in the troposphere by the minimum equilibrium temperature of 200K in Eq. (1). The pattern of the radiative equilibrium temperature at the summer solstice is displayed for $A_0 = 60$ in Fig. 2. Given the thermal damping time scale of 40 days used in the model, this gives a heating rate of $\sim$2 K day^{-1}, which is comparable to the magnitude of the zonally asymmetric heating in the observations (Fig. 2 of *Hazra and Krishnamurthy* [2015]). In the boundary layer of the Held-Suarez configuration, the thermal damping time scale transitions to very short values near the surface to account for the lack
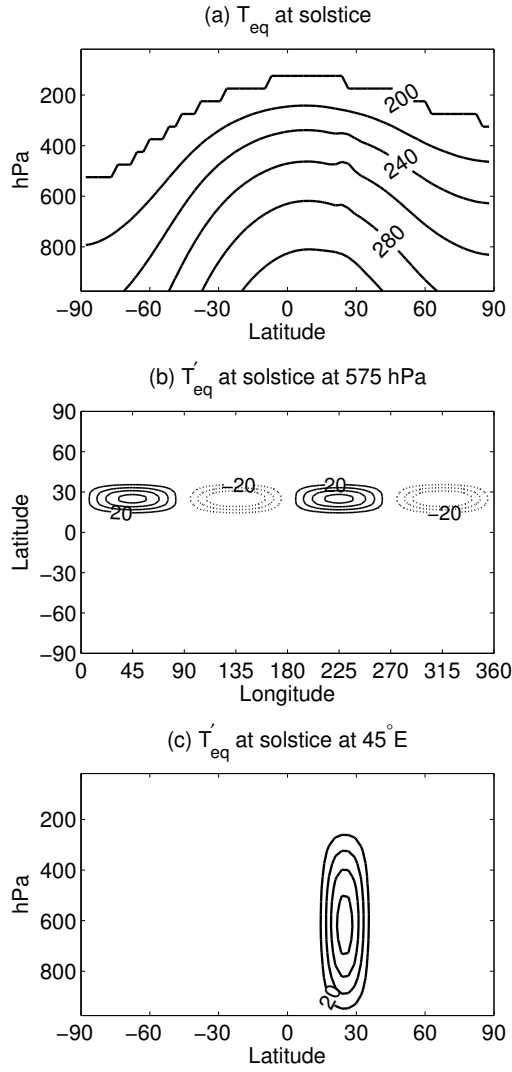
Figure 2. Prescribed radiative equilibrium temperature (K), T_{eq}, at the summer solstice for A_0=60: (a) zonally averaged T_{eq}, (b) the horizontal cross section of T'_{eq} at 575 hPa, and (c) meridional cross section of T'_{eq} at 45° longitude. T'_{eq} denotes the deviation from the zonal mean. See Eqs. (1) and (2) for details.

Table 1. Descriptions of idealized experiments. A_0 denotes the amplitude of zonally asymmetric heating. p_b is the top boundary of the source region Ω_{MID}. α_{eddy} denotes the strength of eddy mixing. Γ is the mean age at 15°S/80°S and 875 hPa since last contact with the NH boundary layer (e.g., 3.1/3.5 denotes the mean age of 3.1 years at 15°S and 3.5 years at 80°S). See section 2 for details.

| Expt	Brief Description	$\hat{t}$ in T_{eq}	A_0 in T'_{eq}	p_b (hPa)	α_{eddy}	Γ (year) at 15°S/80°S
1	no seasonal cycle	equinox	0	800	1.0	3.1/3.5
2a	seasonal & zonally symmetric	seasonal	0	800	1.0	2.6/3.1
2b	seasonal & monsoon forcing	seasonal	10	800	1.0	2.4/2.9
2c	seasonal & monsoon forcing	seasonal	20	800	1.0	2.3/2.8
2d	seasonal & monsoon forcing	seasonal	30	800	1.0	2.1/2.6
2e	seasonal & monsoon forcing	seasonal	40	800	1.0	2.0/2.5
2f	seasonal & monsoon forcing	seasonal	50	800	1.0	1.9/2.4
2g	seasonal & monsoon forcing	seasonal	60	800	1.0	1.8/2.3
3a	varied source region depth	seasonal	60	700	1.0	1.6/2.1
3b	varied source region depth	seasonal	60	900	1.0	2.4/2.9
4a	eddy/mean flow partitioning	seasonal	60	800	0	7.2/6.7
4b	eddy/mean flow partitioning	seasonal	60	800	0.5	2.3/2.5
4c	eddy/mean flow partitioning	seasonal	60	800	2.0	1.6/1.8

of surface heat and momentum fluxes, which may produce unrealistic diabatic heating rates there.

A series of idealized experiments are conducted and summarized briefly in Table 1. Experiment 1 is simulated under perpetual equinoctial zonally symmetric heating. This is in contrast to experiment 2a under seasonally-varying zonally symmetric heating, which is used to assess the impact of the seasonal migration of the Hadley cell on interhemispheric transport. Next, experiments 2a-2g are performed using the same seasonally-varying zonally symmetric heating, but the amplitude of zonally asymmetric heating increases from $A_0 = 0$ to $A_0 = 60$ at an increment of 10.

The model simulations are run at T42 horizontal resolution with 20 equally spaced sigma levels in the vertical. The subgrid-scale diffusion is parameterized by the ∇^4 hyperdiffusion on temperature, vorticity, and divergence, with the diffusion coefficient of 1.0×10^{16} m^4 s^{-1}. For the tracer diagnostics, a grid tracer is used with a semi-Lagrangian scheme for horizontal advection [*Lin et al.*, 1994] and a finite-volume parabolic scheme for vertical advection. A global mass fixer, that rescales the global tracer mass at every time step [*Orbe et al.*, 2012], is used to ensure that the global tracer mass remains unchanged by advection. While this does not fix local numerical errors in tracer advection, this ensures global tracer mass conservation. There is no explicit numerical diffusion applied to the grid tracer. Note that we have used a spectral version of the tracer with explicit hyperdiffusion and find that the results are quantitatively similar to the grid tracer. Unlike *Orbe et al.* [2016], there is no convective parameterization in this idealized model and thus no convective tracer transport; the short radiative relaxation time scale near the surface may also produce unrealistic near-surface diabatic transport. All of the simulations are run for 20 years, with the first 5 years as the spinup.

2.2 Atmospheric circulations

The atmospheric circulations simulated in the model are exemplified by experiment 2g in Fig. 3, which is forced by seasonally-varying zonally symmetric heating as well as the monsoon-like zonally asymmetric heating (A_0=60). In the NH, the upper-tropospheric zonal

(a) seasonal T_{eq} & T'_{eq} at 45°E, at 575 hPa

(b) u at 375 hPa

(c) v at 375 hPa
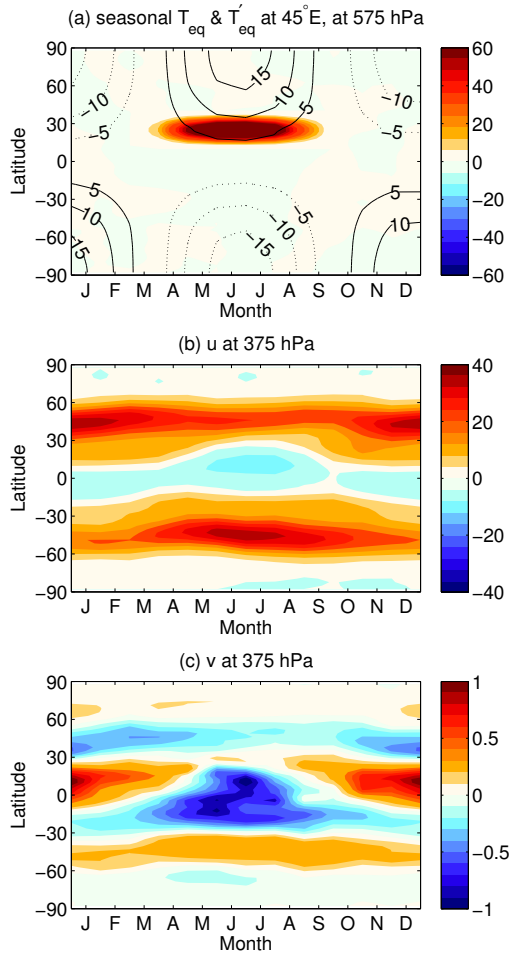
Figure 3. Seasonal evolution of atmospheric circulations for the experiment forced by seasonally-varying zonally symmetric heating as well as the monsoon-like zonally asymmetric heating for A_0=60 (expt 2g in Table 1): (a) anomalous (i.e., annual mean-removed) zonal mean radiative equilibrium temperature T_{eq} (contours; K) and T'_{eq} at 45° longitude (shading; K) at 575 hPa, (b) zonal mean zonal wind at 375 hPa (m s^{-1}), and (c) zonal mean meridional wind at 375 hPa (m s^{-1}).

mean zonal winds exhibit a seasonal transition from a strong wintertime jet to a weak summertime jet, associated with a change from a northward upper-level cross-equatorial flow in winter to a southward cross-equatorial flow in summer. The SH displays a similar seasonal transition with a lag of six months, as expected from the lag in the seasonal cycle of the radiative forcing. In addition, the zonally asymmetric heating in the NH subtropics is used to mimic the heating anomaly associated with Asian and North American monsoons. This yields a hemispheric asymmetry between the summertime circulations in the two hemispheres, with slightly stronger easterlies and cross-equatorial flow at ~10°N in comparison with their SH counterpart at ~10°S.

The effect of the zonally asymmetric heating is highlighted by contrasting the July mean circulations simulated in experiments 2a (A_0=0) and 2g (A_0=60) in Fig. 4. The prescribed zonally asymmetric heating generates planetary waves that give rise to an upward lift in the Hadley circulation near 20°N and enhanced upper-tropospheric angular momentum transport from tropical easterlies to midlatitude westerlies. This is, however, secondary as compared with the pronounced zonal asymmetry in circulation. The imposed warming leads
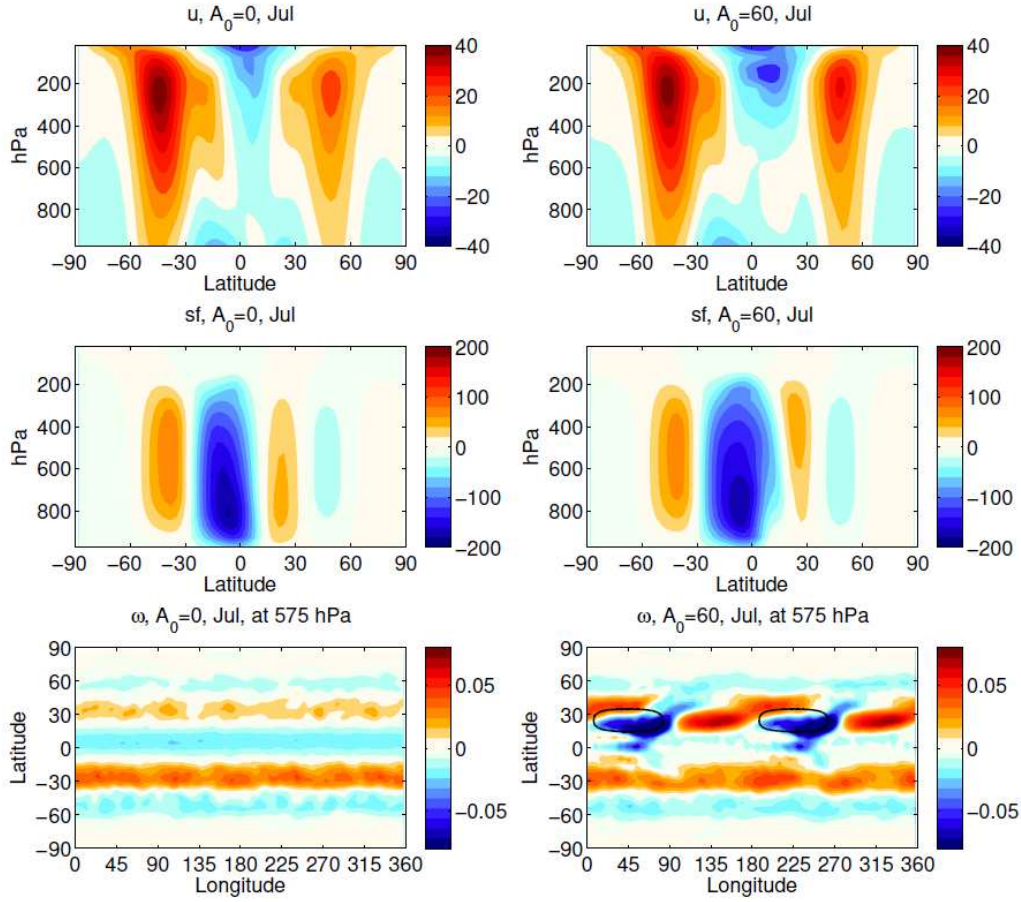
Figure 4. July mean circulations for the simulations (left) without and (right) with the zonally asymmetric heating, i.e., A_0=0 and 60 (expts 2a and 2g), respectively: (top) zonal mean zonal wind (m s^{-1}), (middle) mean meridional streamfunction (10^9 kg s^{-1}), and (bottom) pressure vertical velocity at 575 hPa (Pa s^{-1}). Black circles in the bottom right panel indicate the region of local warming (cf. Fig. 2).

to strong upward motion locally that is accompanied by remote descent to the west of warming. All these characteristics are consistent with *Zhai and Boos* [2015], who examine the monsoonal circulation response to perpetual local subtropical heating. The streamfunction maximum in Fig. 4 is comparable in magnitude with observations (Figs. 1 and 5 of *Dima and Wallace* [2003]), and the seasonal forcing used here is similar to the sinusoidal temporal variation in the leading mode of the Hadley cell. Adding the monsoon-like heating alters the structure of the Hadley cell, but it does little to the magnitude of the streamfunction. Therefore, it allows us to approximately separate the seasonal migration of the Hadley cell from the zonally asymmetric monsoon circulation. However, given the simplicity of the model configuration, one should bear in mind that there exist differences in the structure of the Hadley cell between this idealized model and observations.

2.3 Diagnostic of transport

While interhemispheric transport has traditionally been expressed in terms of the hemispherically averaged time obtained using a two-box model [e.g., *Levin and Hesshaimer*, 1996; *Geller et al.*, 1997], we quantify interhemispheric transport in terms of the mean age of air and transit time distribution since last contact at the NH midlatitude surface [*Waugh*

et al., 2013; *Holzer and Waugh*, 2015; *Orbe et al.*, 2016]. This follows the theory of the age of stratospheric air since last contact at the tropical tropopause (see the review by *Waugh and Hall* [2002]), but redefines the boundary condition as the NH midlatitude surface. Unlike the path density diagnostic [*Holzer*, 2009a,b], this does not include the path information of where individual air masses pass en route to the SH.

More specifically, let us consider the transit time distribution corresponding to a conserved and passive tracer of mixing ratio $\chi(\mathbf{r}, t)$, where transit time refers to the elapsed time $\tau \equiv t - t'$ since the air at a location r and time t was last over the NH midlatitude source region at time t', denoted by Ω_{MID} and defined here as all gridpoints between 30°N and 50°N from the surface to the top boundary at $p_b = 800$ hPa. The tracer mixing ratio in the source region Ω_{MID} at time t' is specified as $\chi(\Omega_{\text{MID}}, t')$, and its value is constant in Ω_{MID} to mimic the effect of the boundary layer turbulent mixing in more realistic models. There is no source or sink of tracer outside the Ω_{MID} region. Experiments 3a (p_b=700 hPa) and 3b (p_b=900 hPa) are conducted to examine the sensitivities of tracer transport to the top boundary of Ω_{MID} and are discussed at the end of section 3.

Given a Green function $\mathcal{G}(\mathbf{r}, t|\Omega_{\text{MID}}, t')$ that satisfies the tracer advection equation and the boundary condition $\mathcal{G}(\Omega_{\text{MID}}, t|\Omega_{\text{MID}}, t') = \delta(t - t')$, where $\delta(t - t')$ denotes a delta function, the tracer mixing ratio at the position $\mathbf{r}$ and time t can be written as

$$
\begin{aligned}
\chi(\mathbf{r}, t) &= \int_{-\infty}^{t} \chi(\Omega_{\text{MID}}, t')\mathcal{G}(\mathbf{r}, t|\Omega_{\text{MID}}, t')dt' \\
&= \int_{0}^{\infty} \chi(\Omega_{\text{MID}}, t - \tau)\mathcal{G}(\mathbf{r}, \tau|\Omega_{\text{MID}})d\tau
\end{aligned}
\tag{4}
$$

Hence $\mathcal{G}(\mathbf{r}, t|\Omega_{\text{MID}}, t')$ "propagates" the mixing ratio in the source region Ω_{MID} at time t' to the point $\mathbf{r}$ at time t. The Green function or TTD is rewritten as $\mathcal{G}(\mathbf{r}, \tau|\Omega_{\text{MID}}) = \mathcal{G}(\mathbf{r}, t|\Omega_{\text{MID}}, t - \tau)$ under the assumption that the flow is cyclostationary and the dependence on t is dropped. If the tracer mixing ratio in the source region is specified as $\chi(\Omega_{\text{MID}}, t') \equiv 1$, it is expected that the tracer field will be homogenized eventually, and this yields $\chi(\mathbf{r}, \infty) = \int_{0}^{\infty} \mathcal{G}(\mathbf{r}, \tau|\Omega_{\text{MID}})d\tau = 1$. Therefore, $\mathcal{G}(\mathbf{r}, \tau|\Omega_{\text{MID}})d\tau$ can be thought of as the mass fraction of the air parcel at the position $\mathbf{r}$ and time t that was last in contact with the source region Ω_{MID} between the transit time τ and $\tau + d\tau$.

The mean age of air at the position $\mathbf{r}$ since last contact with the source region Ω_{MID} can be defined by the first moment of the TTD

$$
\Gamma(\mathbf{r}|\Omega_{\text{MID}}) \equiv \int_{0}^{\infty} \tau \mathcal{G}(\mathbf{r}, \tau|\Omega_{\text{MID}})d\tau,
\tag{5}
$$

and the spectral width of the TTD is defined by its second moment

$$
\Delta(\mathbf{r}|\Omega_{\text{MID}}) \equiv \sqrt{\frac{1}{2} \int_{0}^{\infty} [\tau - \Gamma(\mathbf{r}|\Omega_{\text{MID}})]^2 \mathcal{G}(\mathbf{r}, \tau|\Omega_{\text{MID}})d\tau}.
\tag{6}
$$

From a one-dimensional advection-diffusion model with constant advective velocity and diffusivity, the analytic solution of the TTD can be expressed as an inverse Gaussian distribution, $\mathcal{G}(\tau) = \frac{1}{2\Delta\sqrt{\pi \hat{\tau}^3}} \exp[-\frac{\Gamma^2(\hat{\tau}-1)^2}{4\Delta^2 \hat{\tau}}]$ with $\hat{\tau} = \tau/\Gamma$, where Γ, Δ, and τ are the mean age, spectral width, and transit time, respectively [e.g., *Waugh and Hall*, 2002]. The TTD of a tracer subject to pure advection is simplified to a delta function centered at the time scale that is determined by the mean advection; enhanced tracer mixing broadens the TTD, leading to younger modal age and longer tail of old air (see Fig. 3 of *Waugh and Hall* [2002]). Hence, the ratio Δ/Γ, referred to as the shape parameter, can , at least partly, characterize the long tail of the TTD in this analytic solution, and thus it will be used to assess the contribution of slow eddy-diffusive recirculations relative to fast advective transport.

The TTD diagnostics are computed in the same way as *Orbe et al.* [2016] to facilitate the comparison with the GMI-MERRA simulation. Idealized Boundary Impulse Response

(BIR) tracers are implemented to approximate the Green function response to a boundary layer delta function forcing. After a 5 year spin-up, four BIR tracers are released in the Ω_{MID} region every three months for a duration of 1 day at the value of 1 and then held at zero for the rest of the integration. Setting the tracer back to zero in the source region acts as a sink of the tracer, and thus the BIR tracer decays with time after the initial pulse. For the runs subject to the seasonal radiative forcing, four BIR tracers are released on the first day of January, April, July, and October, respectively. While the instantaneous variations of TTD and BIR are different for a non-stationary flow and the distinctions may be important for the annual cycle of the TTD, the TTD and BIR have identical statistics in the long term mean. Thus, the average of four BIR tracers centered about the transit time $\tau = 0$ is used to estimate the annual mean statistics of TTD, although more BIR tracers may be needed to recover the exact TTD in a turbulent flow [*Haine et al.*, 2008]. The exponential tail of the TTD near and above the tropopause, where the mean age is large, is extrapolated to account for the limited length of the simulation. Finally, the accuracy of the BIR approach for computing the mean age is verified by a clock tracer, which is held at zero in the source region Ω_{MID} and is aged at a rate of 1 year per year outside Ω_{MID} [*Waugh et al.*, 2013; *Orbe et al.*, 2016]. An ideal age is obtained as the 5-year average of the clock tracer after 15 years of integration, when the clock tracer has equilibrated almost everywhere in the troposphere. The mean age from the BIR tracers agrees quantitatively with the ideal age from the clock tracer, and thus the latter is not shown here.

2.4 Mean mass transport versus eddy mixing

The effect of mean mass transport versus eddy mixing is diagnosed using the method described in *Chen and Plumb* [2014]. For a tracer of mixing ratio χ, the mean mass transport and eddy mixing may be separated as

$$\frac{\partial \chi}{\partial t} = -\frac{1}{\rho}\nabla \cdot (\rho \mathbf{u}\chi) = -\frac{1}{\rho}\nabla \cdot (\rho \alpha_{mean}\mathbf{u}_{res}\chi) - \frac{1}{\rho}\nabla \cdot [\rho \alpha_{eddy}(\mathbf{u} - \mathbf{u}_{res})\chi] \qquad (7)$$

where ρ is density, ∇ is a 3D gradient operator, and $\mathbf{u} = (u, v, w)$ is the 3D velocity. For illustration purposes we assume the flow is incompressible, $\nabla \cdot (\rho \mathbf{u}) = 0$. $\mathbf{u}_{res} = (0, v_{res}, w_{res})$ denotes the zonal mean residual meridional circulation, and it is calculated at every time step on the model grid to satisfy mass conservation, $\nabla \cdot (\rho \mathbf{u}_{res}) = 0$. As such, the contribution of mean mass transport versus eddy mixing to tracer transport can be illuminated by modifying the parameters α_{mean} and α_{eddy}, respectively. As shown in *Chen and Plumb* [2014], in the limit of $\alpha_{mean} = 1$ and $\alpha_{eddy} = 0$, the tracer is advected only by the residual circulation, and the tracer is expected to be homogenized along the streamline of the zonal mean residual circulation. Conversely, in the limit of $\alpha_{mean} = 0$ and $\alpha_{eddy} = 1$, the tracer is advected by eddy stirring but with no diabatic mass transport, and the tracer is expected to be homogenized along isentropic surfaces. By varying the value of α_{eddy} from 0 to 2, experiments 4a-4c are performed to examine the effect of slow eddy-diffusive recirculations on tracer transport in section 4.

3 Transit Time Distribution (TTD)

The spatial pattern of interhemispheric transport is described by the TTDs at different pressure levels and latitudes, approximated by the average of four BIR tracers released in the NH midlatitude boundary layer Ω_{MID} on January 1, April 1, July 1, and October 1, respectively. Figure 5 gives the TTDs in the upper troposphere (375 hPa) and near the surface (875 hPa) for experiments 1 (black), 2a (blue), and 2g (red). The latitude 15°S and 15°N are selected to capture the meridional gradient in the cross-equatorial transport, and 80°S is chosen to represent the SH high latitudes. Overall, the TTD in the idealized model is characterized by a large peak (modal age) at young transit times and a long flat tail of old air, as found in the GMI-MERRA model [*Orbe et al.*, 2016]. In the tropics, the TTDs are heavily skewed to young transit times, whereas the TTDs in the SH high latitudes are less skewed and closer to
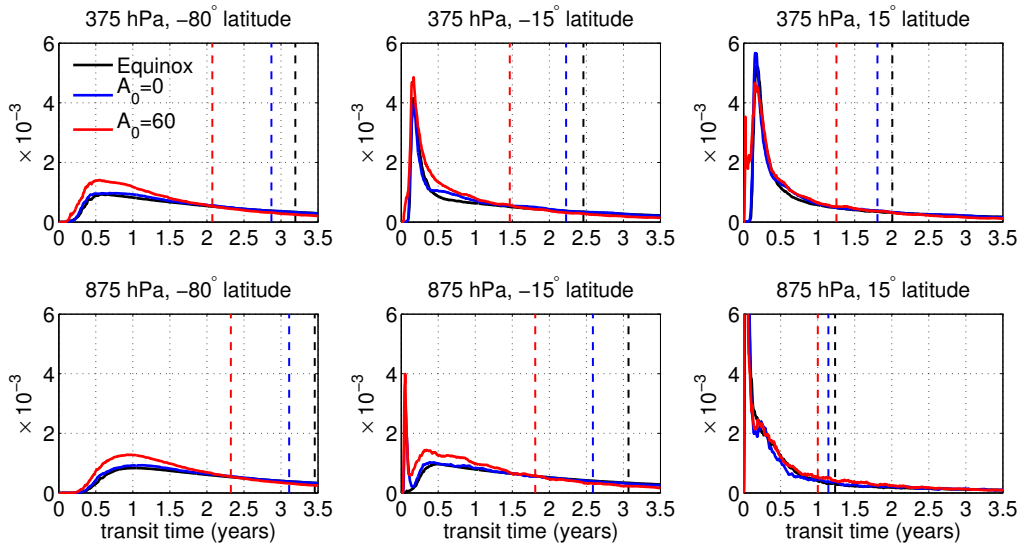
Figure 5. Zonally averaged Transit Time Distributions (TTDs) since last contact with the NH midlatitude boundary layer Ω_{MID} for the simulations (blue) without and (red) with the zonally asymmetric heating, i.e., expts 2a (A_0=0) and 2g (A_0=60), respectively, and (black) under the perpetual equinoctial radiative forcing (expt 1). The TTD is approximated by the average of four Boundary Impulse Response (BIR) tracers released in Ω_{MID} at the source time t'= January 1, April 1, July 1 and October 1, plotted relative to the transit time $\tau = t - t'$, where t is the sample time. The location of each TTD is indicated by pressure and latitude in each subplot. Dashed vertical lines indicate the mean age of each TTD.

the inverse Gaussian distribution with the disappearance of young air ($\tau < 50$ days). As such, while the modal age captures the peak at young transit times, the mean age is much larger than the modal age due to the highly skewed TTD.

As reviewed in the introduction, interhemispheric transport can be influenced by both the seasonal cycle of the Hadley circulation [*Bowman and Cohen*, 1997] and eddy-diffusive recirculations. The former can be attributed to seasonally-varying zonally symmetric heating, and the latter may be driven by the monsoonal circulation or some other zonally asymmetric forcing. The comparison of different simulations in Fig. 5 shows that the monsoon-like zonally asymmetric heating (experiment 2a with $A_0 = 0$ vs. 2g with $A_0 = 60$) is more efficient for transport across the equator than the seasonal migration of the Hadley cell (experiment 1 vs. 2a). Particularly, the seasonal, zonally symmetric heating reduces the mean age at 80°S and 875 hPa from ~3.5 years to ~3.1 years, and the zonally asymmetric heating produces additional reduction to ~2.3 years. The larger influence on the age of tropospheric air by the zonally asymmetric heating than the seasonal, zonally symmetric heating is also evident at other pressure levels and latitudes.

The spatial structure of TTD characteristics is summarized by four metrics in Fig. 6: the mean age Γ, modal age τ_{mode}, spectral width Δ, and shape parameter Δ/Γ since last contact with the source region Ω_{MID}. In the source region of 30-50°N and below 800 hPa, $\Gamma = 0$ and $\Delta = 0$ by definition, that is, the transit time is reset to zero when the isentropic recirculation travels from the tropics to the NH high latitudes through this region. Hence, in most of the NH extratropics this yields a large peak of young air with very short modal age (< 10 days, noting the logarithmic scale). For the isentropic surface closer to the source region, the recirculation is more likely relabeled as young air, and thus the spatial pattern of the mean age resembles that of the spectral width, reflecting the change in the long tail of old air with

respect to the isentropic surface in the NH. In contrast, in the SH extratropics the gradient in the spectral width is small and the spatial pattern of the mean age is more similar to that of the modal age, reflecting the gradual disappearance of fast transport paths from the SH subtropics to the South Pole (also see Fig. 5). As a result, the spectral width relative to the mean age is broad (i.e., $\Delta/\Gamma > 1$) in the NH and narrow (i.e., $\Delta/\Gamma < 1$) in the SH. In spite of the simplicity of the idealized model, these above features agree well with the GMI-MERRA simulation (Fig. 2 of *Orbe et al.* [2016]) and thus underscore the importance of large-scale atmospheric circulations in setting up the transport climate.

On the other hand, the mean age at the equator displays a sharp meridional gradient in contrast to strong vertical gradients in modal age. This vertical gradient in modal age differs from the meridional gradient found in the GMI-MERRA simulation [*Orbe et al.*, 2016], which can be attributed to the lack of convection and associated vertical mixing in this idealized dry model that would otherwise mix the modal age vertically by convective transport. The similarity of the cross-equatorial meridional gradient between the mean age and spectral width in the idealized model again indicates the importance of recirculations in interhemispheric transport. In more realistic models, interhemispheric transport can be further enhanced by convection and vertical mixing [e.g., *Gilliland and Hartley*, 1998].

The TTD response to the monsoon-like zonally asymmetric heating is illuminated by comparing the left and right columns of Fig. 6 (experiment 2a with $A_0 = 0$ vs. 2g with $A_0 = 60$). The mean age becomes younger throughout the troposphere, with the largest reduction in the age gradient occurring in the tropics. In contrast to the spatial pattern of climatological mean age varying with the spectral width only in the NH, this reduction in mean age by the zonally asymmetric heating is associated with narrower spectral width throughout the troposphere. Noting as the amplitude of zonally asymmetric heating increases from $A_0=0$ to $A_0=60$, the mean age in the SH subtropics/high latitudes at 875 hPa decreases from 2.6/3.1 years to 1.8/2.3 years, respectively (Table 1). This results in a mean age that agrees better with observational-based estimates of mean age of around 1.1 years in the SH subtropics and 1.4 years in SH high latitudes [*Waugh et al.*, 2013; *Holzer and Waugh*, 2015] and the spatial pattern in the GMI-MERRA simulation [*Orbe et al.*, 2016], although additional processes such as convective mixing are needed to produce realistic values in mean age. In contrast, there is little change in the modal age and shape parameter except for the modal age near 20°N latitude where the zonally asymmetric heating is imposed. These suggest that the monsoon-like zonally asymmetric heating has a larger influence on slow recirculations (spectral width) compared to fast advective transport (modal age).

It is worthwhile revisiting the impact of the seasonal migration of the Hadley circulation on interhemispheric transport [*Bowman and Cohen*, 1997]. Figure 7 gives the TTD characteristics in the simulation in which the radiative equilibrium temperature is fixed to the perpetual equinoctial condition, and thus the upward branch of the Hadley cell stays near the equator, as evident in the patterns of the mean age, spectral width and shape parameter. While the overall patterns of the TTD metrics in the extratropics are qualitatively similar, the absence of the seasonal migration in the Hadley cell leads to an older mean age and wider spectral width in the SH. This indicates a slowdown in the recirculation of old air, presumably resulting from the perpetual updraft at the equator. Again, the seasonal migration in the Hadley cell has little impact on the structure of the modal age.

The robustness of the relationship described above is verified by plotting individual metrics as a function of the heating amplitude at selected locations in the tropics and the SH high latitudes (Fig. 8). The mean age and spectral width at the selected locations display a decreasing trend with a larger heating amplitude, and their decreases in the SH are comparable in magnitude with the reduction in the NH tropical upper troposphere. In contrast, the modal age as well as the shape parameter exhibits little sensitivity to the heating amplitude (also see Fig. 5).
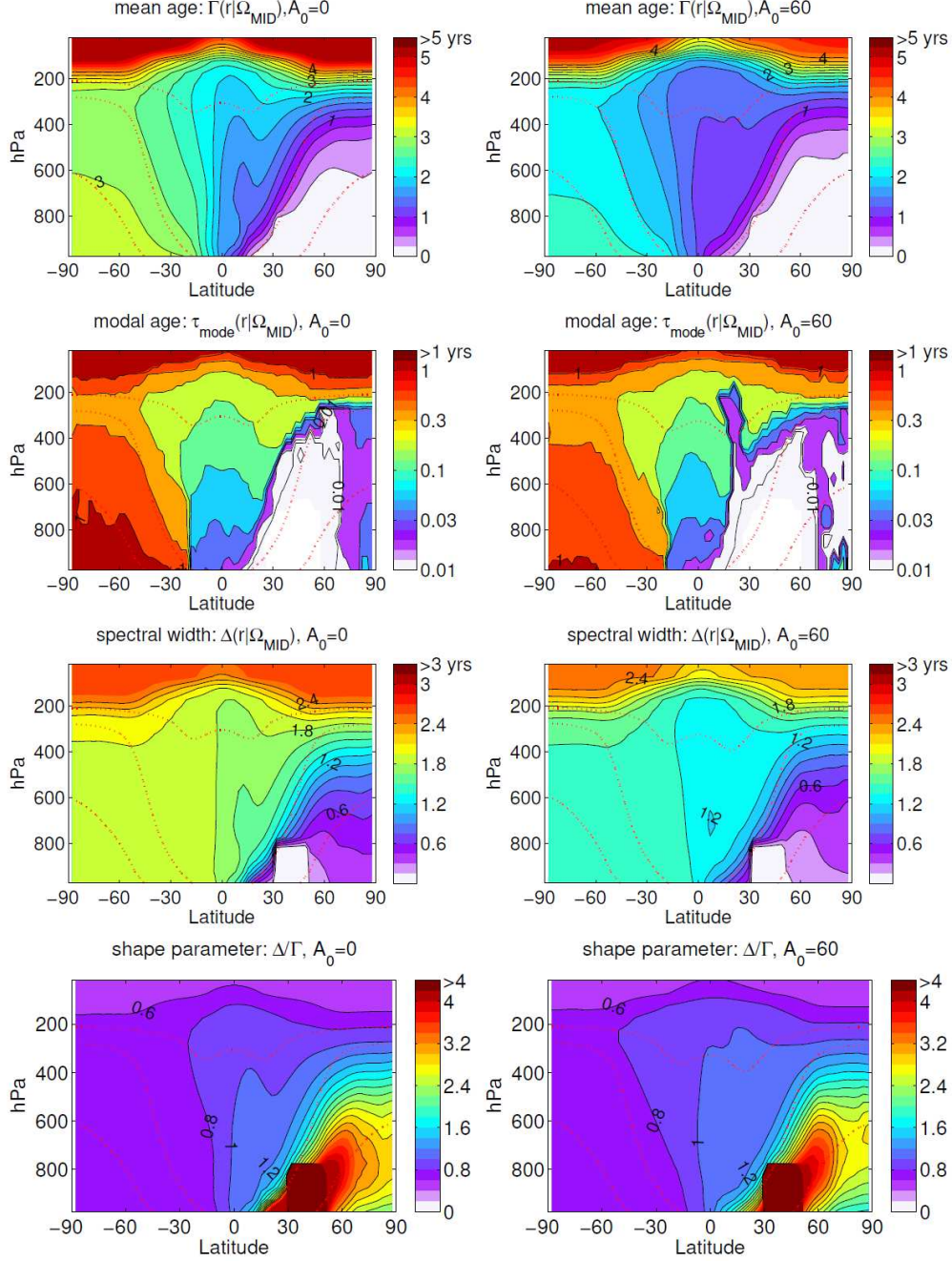
Figure 6. Zonally averaged mean age (Γ; year), modal age (τ_{mode}; year), spectral width (Δ; year), and shape parameter (Δ/Γ) of the TTDs since last contact with Ω_{MID} for the simulations (left) without and (right) with the zonally asymmetric heating (expts 2a with A_0=0 and 2g with A_0=60). Red dotted lines denote the 280K, 300K and 320K isentropes. Note the log scale in τ_{mode}.
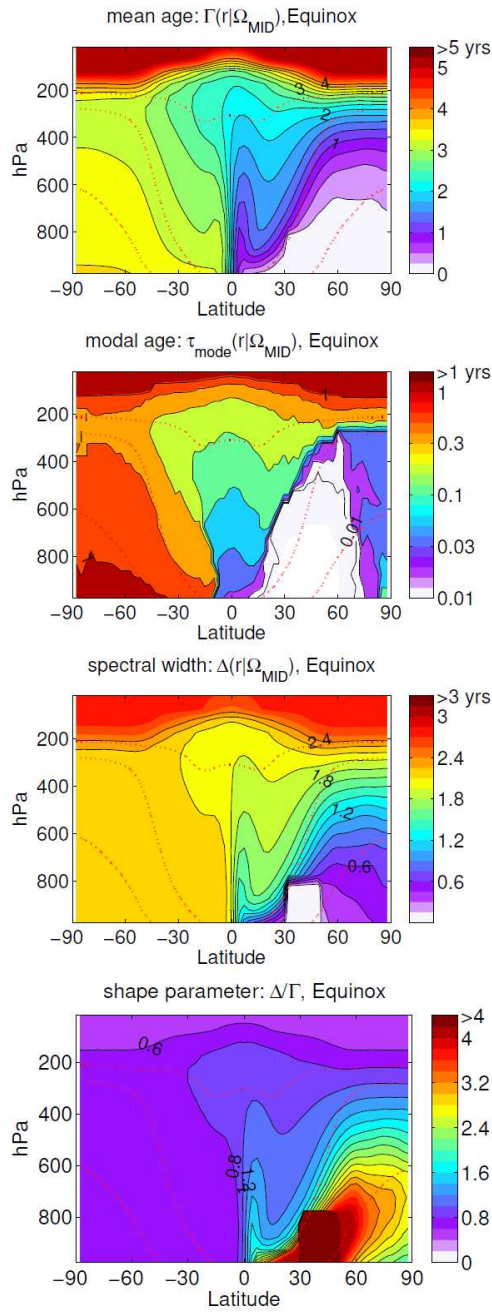
Figure 7. As in Fig. 6, but for the simulation under the perpetual equinoctial radiative forcing (expt 1).
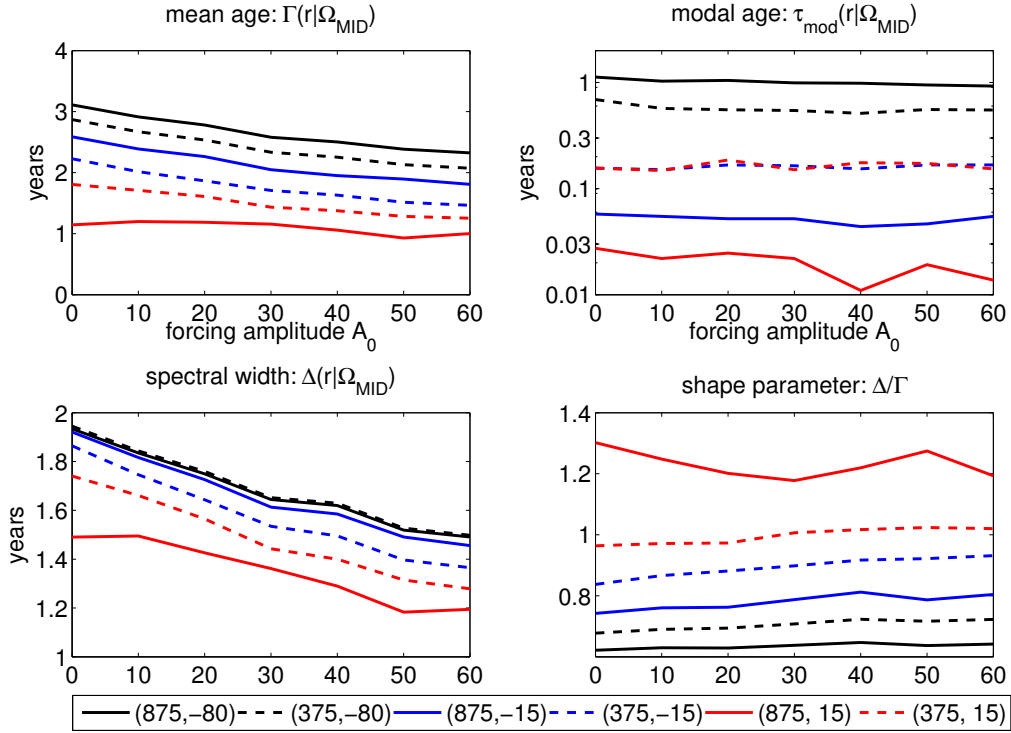
Figure 8. Mean age (Γ; year), modal age (τ_{mode}; year), spectral width (Δ; year), and shape parameter (Δ/Γ) of the TTDs since last contact with Ω_{MID} as a function of the amplitude of zonally asymmetric heating. The location of each metric is indicated in the parentheses as (hPa, degrees latitude). Note the log scale in τ_{mode}.
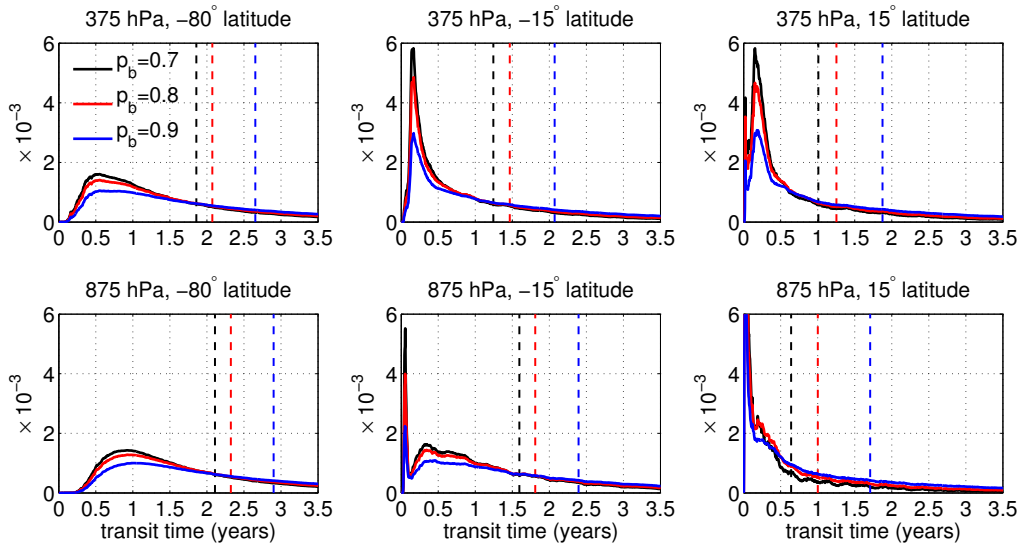
Figure 9. As in Fig. 5, but for varied top boundaries in Ω_{MID} as $p_b = 700, 800,$ and 900 hPa (i.e., expts 3a, 2g, and 3b), respectively.

In light of the above role of slow recirculations in determining the mean age and spectral width, we further examine the sensitivities of the TTD to the top boundary of the source region (Fig. 9). As the isentropic recirculation moves from the tropics to the NH high latitudes, old air is relabeled as young air in the source region, and thus a rise in the top boundary of the source region is likely to remove more recirculating old air at the tail of the TTD. Indeed, in response to a deeper source region, the TTD exhibits an increase in short transit times and a decrease at the long tail, and the decrease in mean age in the SH is comparable in magnitude with that in the NH tropical upper troposphere. Therefore, the similar change in the TTD in the SH between Figs. 5 and 9 supports the notion that the increased interhemispheric exchange in response to the zonally asymmetric heating may be attributed to accelerated recirculations.

4 Transport pathways

The BIR tracers released in four seasons are now compared with one another. This allows us to decompose the annual mean BIR or TTD in Fig. 5 by season, and thus to relate the TTD change to the seasonal change in the transport pathways associated with the Hadley cell or the monsoon [*Holzer*, 1999; *Orbe et al.*, 2016]

The seasonal variation of the Hadley cell (Fig. 3) is characterized by the latitudinal shift of its upward branch from the SH in January to the NH in July. This latitudinal shift influences the location and season of the largest response among the four BIR tracers, as evident from the simulation driven by seasonally-varying zonally symmetric heating in Fig. 10: the January tracer (i.e., the BIR tracer released at the source time of January 1) exhibits a notable increase in the SH tropical lower troposphere (Fig. 10e), whereas the July tracer displays a pronounced increase in the NH tropics (Fig. 10c and f), as expected from the latitude of the upward branch of the Hadley cell. It is noteworthy that the mean age in the SH tropical upper troposphere is smaller than that of the same latitude in the lower troposphere (Figs. 6 and 7), and thus the primary cross-equatorial transport takes place through the upper troposphere rather than the lower troposphere. This has been noted by many previous studies [e.g., *Plumb and Mahlman*, 1987; *Holzer*, 1999; *Bowman and Erukhimova*, 2004]. It is then surprising that the July tracer in Fig. 10e yields the smallest increase among the four seaso-
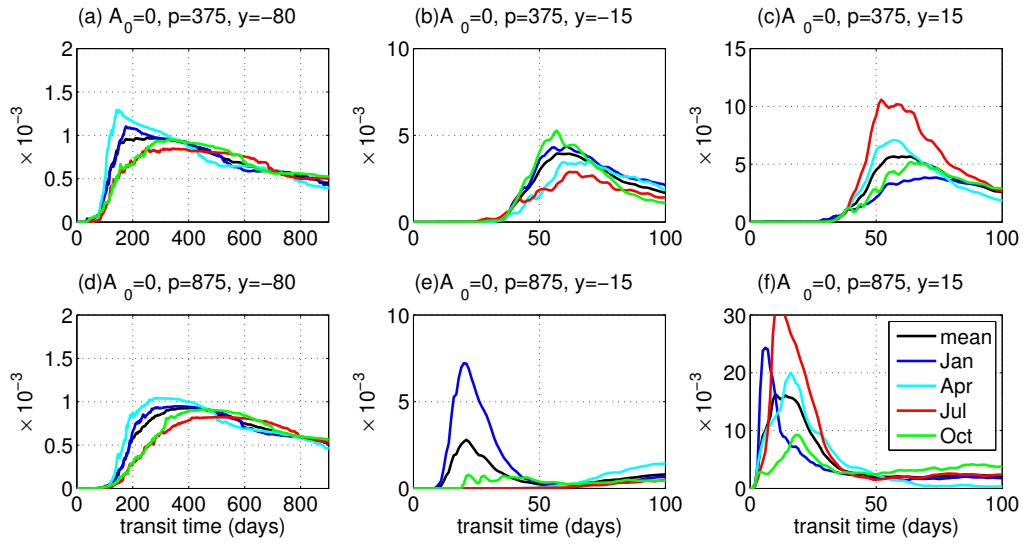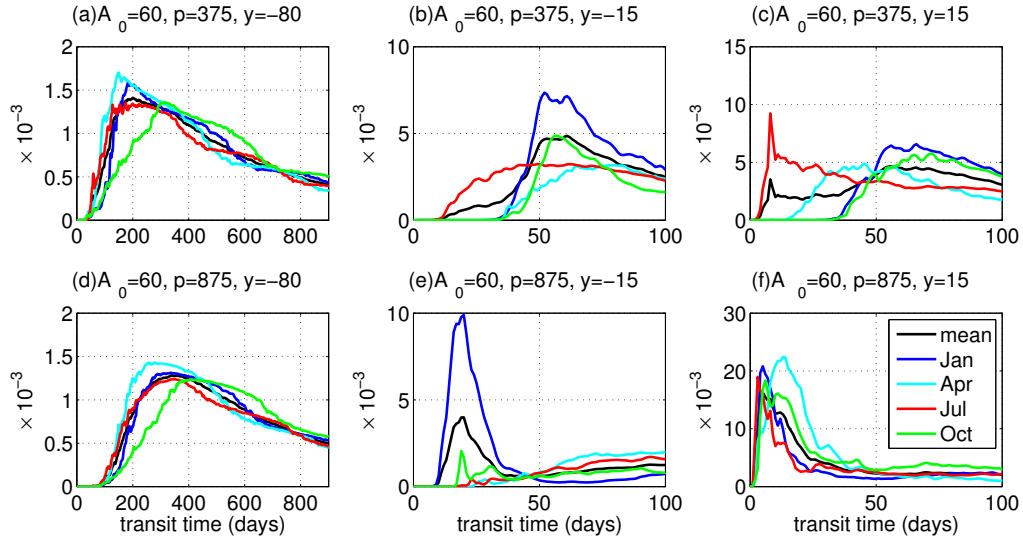
Figure 10. Zonally averaged BIR tracers since last contact with Ω_{MID} for the simulation with seasonally-varying zonally symmetric heating (expt 2a). The BIR tracers are released at the source time t' = January 1 (blue), April 1 (cyan), July 1 (red), and October 1 (green), plotted relative to the transit time $\tau = t - t'$, where t is the sample time. The annual mean is plotted in black. The location of each BIR is indicated by pressure p and latitude y in each subplot.

nal BIR tracers in the SH tropical upper troposphere, in contrast to *Orbe et al.* [2016] who found the July tracer exhibits the largest increase in the SH tropical upper troposphere in the GMI-MERRA model (their Fig. 3).

The inconsistency above can be resolved by the simulation with the monsoon-like zonally asymmetric heating in Fig. 11. In comparison with Fig. 10e, the January tracer in Fig. 11e displays a similar, large increase in the SH tropical lower troposphere, but the July tracer produces a faster response (from ∼60 days in Fig. 10c to ∼15 days in Fig. 11c) in the NH tropical upper troposphere, followed by an enhancement in fast transit times (<60 days) in the SH tropical upper troposphere (Fig. 11b). This accelerated upper-tropospheric cross-equatorial transport of the July tracer resembles the boreal summer transport pathway found in the GMI-MERRA simulation (Fig. 3 of *Orbe et al.* [2016]).

The spatial pattern of this July transport pathway is illustrated by plotting the zonally averaged July tracer integrated over selected elapsed time intervals since last contact with the source region. The left column of Fig. 12 depicts a slow tropical upward transport pathway over the time scale of ∼1.5 months along the upward branch of the Hadley cell in boreal summer. With the aid of the zonally asymmetric heating in the right column of the figure, the BIR tracer can reach the upper troposphere at ∼20N within 15 days, which, in turn, is transported to the SH tropical upper troposphere.

Figure 13 displays the horizontal distribution of the BIR tracers in the upper and lower troposphere integrated over the elapsed time intervals from t =16 to 30 days, when large cross-equatorial transport occurs in the zonal mean BIR tracers. In the absence of zonally asymmetric heating, the upward transport of the BIR tracer is slow and the subsequent cross-equatorial transport is limited. In contrast, the zonally asymmetric heating drives an upward motion over the warming center, associated with the convergence in the lower troposphere and divergence in the upper troposphere. This up-and-over transport pathway efficiently mo-

Figure 11. As in Fig. 10, but for the simulation with the zonally asymmetric heating (expt 2g).
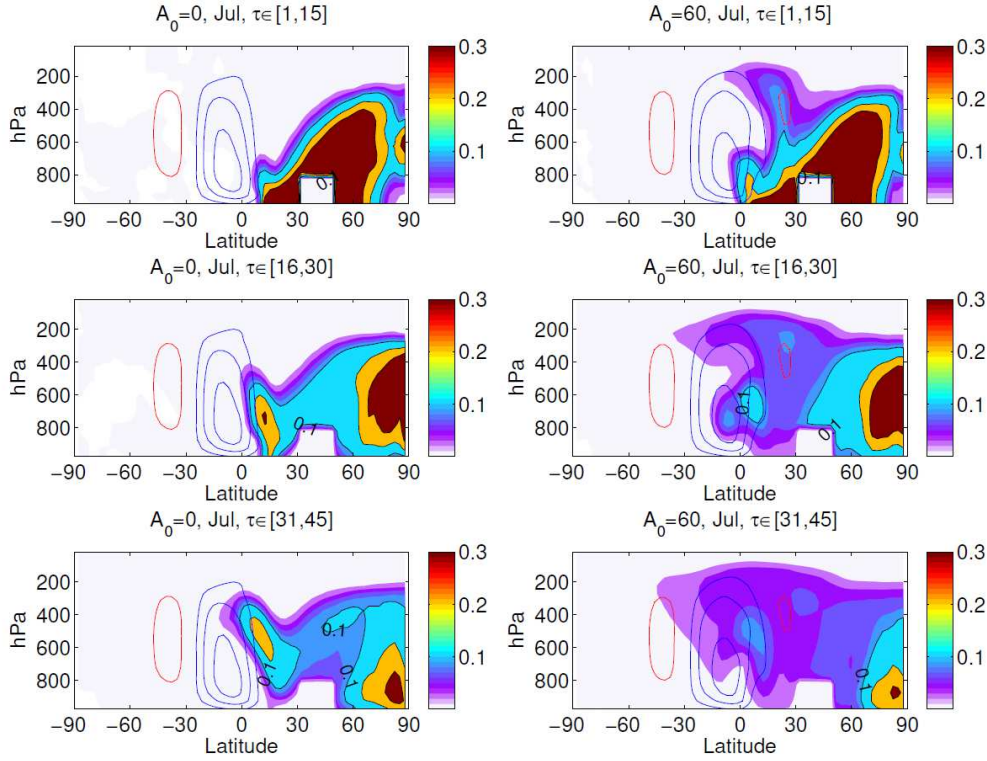

Figure 12. Zonally averaged BIR tracers (shading) integrated over selected elapsed time intervals since last contact with Ω_{MID}, denoted by $\int_{\tau_1}^{\tau_2} BIR(\mathbf{r}, \tau|\Omega_{MID})d\tau$, for the simulations (left) without and (right) with the zonally asymmetric heating (expts 2a and 2g). The time interval $[\tau_1, \tau_2]$ is shown in each subplot. The tracer is released at the source time $t' =$ July 1. Red and blue contours indicate the mean meridional streamfunction in July (cf. the middle panel of Fig. 4).
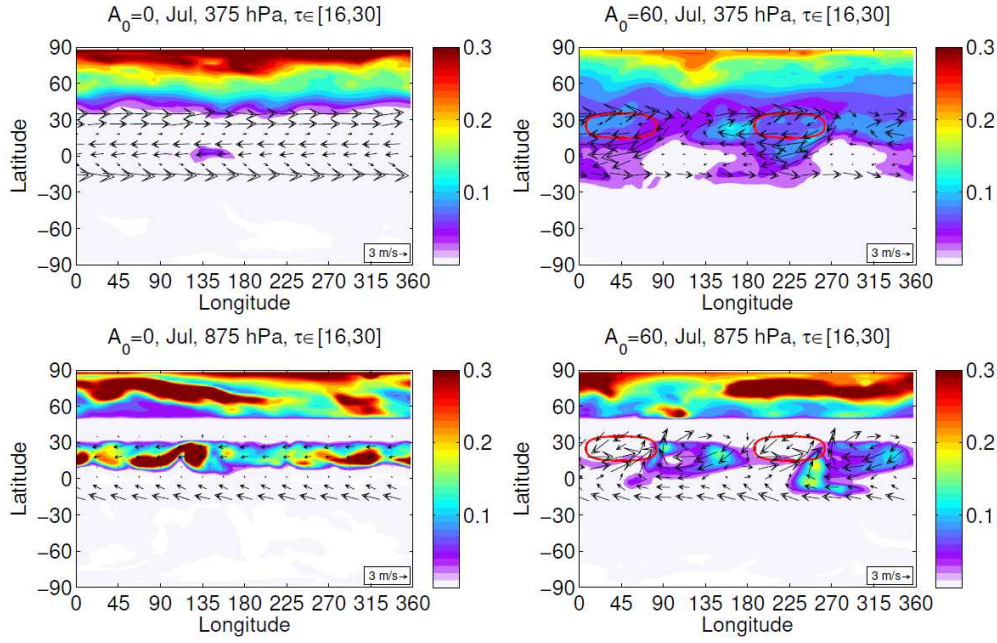
Figure 13. BIR tracers (shading) at 375 hPa and 875 hPa integrated over the elapsed time intervals τ=[16, 30] for the simulations (left) without and (right) with the zonally asymmetric heating (expts 2a and 2g). The tracer is released at the source time t'= July 1, and the horizontal wind vectors represent the climatological mean winds in July. Red circles in the right column indicate the region of local warming.

ves the BIR tracer across the equator through the upper-level anticyclone, which can be assisted by additional eddy shedding associated with the anticyclone [*Popovic and Plumb*, 2001].

One may ask how much of the mean age of air can be attributed to fast advective transport versus slow eddy-diffusive recirculations. The eddy mixing in tracer transport can be separated from the mean mass transport using a method described in section 2.4. Figure 14 gives the mean age from the simulations in which the eddy transport is modified by the factor α_{eddy} = 0, 0.5, 1.0 and 2.0, and the mean residual meridional circulation is fixed by α_{mean} = 1.0. In spite of the seasonal migration of the Hadley cell, the zero mixing limit leads to an age distribution as expected from the transport along the mean residual meridional circulation. In response to enhanced eddy mixing, the meridional gradient in mean age along the NH extratropical isentropic surfaces is reduced; under realistic eddy mixing the isolines of mean age become parallel to the isentropic surfaces. The mean age in the tropics remains to be vertically aligned irrespective of the strength of eddy mixing. As the largest meridional gradient of the mean age is located in the tropics, the change in mean age in the SH follows the change in the NH tropical upper troposphere. This confirms the notion that accelerated eddy-diffusive recirculations lead to enhanced interhemispheric transport and a reduction in mean age in the SH. Interestingly, eddy mixing smooths the separation at ~20°N between the vertically-aligned age isoline in the tropics and the isentropic age isoline in the extratropics (α_{eddy}=0.5 in experiment 4b vs. α_{eddy}=2 in experiment 2g). This is analogous to the impact of the zonally asymmetric heating on the mean age distribution at ~20°N in Fig. 6 (A_0 = 0 in experiment 2a vs. A_0=60 in experiment 2g).
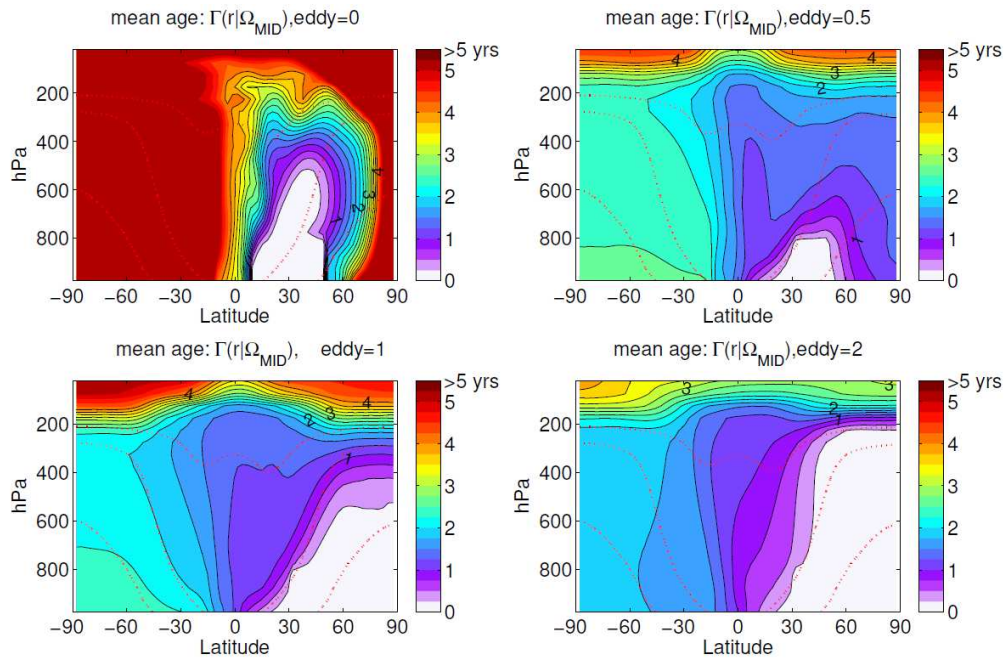
Figure 14. Zonally averaged mean age (Γ; year) of the TTDs since last contact with Ω_{MID} for the simulations in which the strength of eddy mixing is varied by the factor α_{eddy} = 0, 0.5, 1.0 and 2.0 (expts 4a, 4b, 2g, 4c). See Eq. (7) for details.

5 Discussion and Conclusions

While the importance of the seasonal migration of the zonally averaged cross-equatorial flow on interhemispheric transport has been recognized [*Bowman and Cohen*, 1997; *Lintner et al.*, 2004], the role of the zonally asymmetric monsoonal circulation has not been well understood [*Popovic and Plumb*, 2001; *Orbe et al.*, 2016]. This study has investigated the impact of monsoon-like zonally asymmetric heating on interhemispheric transport, using an idealized model of the atmosphere forced by Newtonian relaxation to a prescribed radiative equilibrium temperature. The idealized model allows us to separate the zonally symmetric heating associated with the seasonal cycle of the Hadley cell from the zonally asymmetric heating associated with the monsoon. Interhemispheric transport in the idealized model is assessed by the mean age of air since last contact with the NH midlatitude surface [*Waugh et al.*, 2013; *Orbe et al.*, 2016].

When only zonally symmetric radiative equilibrium temperature is considered, the mean age since last contact with the NH midlatitude boundary layer is unrealistically large as compared with observational-based estimates [*Waugh et al.*, 2013; *Holzer and Waugh*, 2015] and the GMI-MERRA simulation [*Orbe et al.*, 2016]; the introduction of zonally asymmetric heating reduces the mean age to more realistic values. Interestingly, the modal age displays little sensitivity to either the seasonal migration of the Hadley cell or the monsoon-like heating, likely due to the lack of convection and vertical mixing in the idealized model. Furthermore, the zonal asymmetry produces an upper-tropospheric cross-equatorial transport pathway in boreal summer that resembles the transport pathway simulated in the GMI-MERRA model [*Orbe et al.*, 2016]. This transport pathway is linked to the boreal summer monsoon that is characterized by the lower-level convergence and upper-level divergence. A distinct pathway associated with the seasonal migration of the Hadley cell, in contrast, transports air across the equator to the SH in the lower troposphere in boreal winter. In comparison with Fig. 3 of *Orbe et al.* [2016], the difference in timing and altitude of the two trans-

port pathways (as summarized in Fig. 1) highlights the boreal summer monsoon plays an important role in interhemispheric transport.

The idealized simulations also shed light on the important role of eddy-diffusive recirculations on interhemispheric transport. The remove of recirculating old air parcels in the TTD by raising the top boundary of the NH midlatitude source region leads to a decrease in the spectral width and mean age in the SH but with little effect on the modal age. The similar response in TTD to the monsoon-like zonally asymmetric heating (Fig. 5 vs. Fig. 9) suggests that the monsoon may impact the TTD by altering the eddy-diffusive recirculations. A direct acceleration of the eddy mixing in tracer transport leads to enhanced interhemispheric transport and a similar decrease in mean age in the SH (Fig. 14). By analogy, one may also argue that convection and associated vertical mixing [*Gilliland and Hartley*, 1998; *Hess*, 2005; *Erukhimova and Bowman*, 2006] will ventilate the old air associated with slow recirculations and shorten the mean age in the SH since last contact with the NH midlatitude boundary layer, a topic warranting future investigation.

References

Allen, D. R., and N. Nakamura (2001), A seasonal climatology of effective diffusivity in the stratosphere, *Journal of Geophysical Research*, *106*(D8), 7917–7935, doi: 10.1029/2000JD900717.

Bowman, K. P., and G. D. Carrie (2002), The Mean-Meridional Transport Circulation of the Troposphere in an Idealized GCM, *Journal of the Atmospheric Sciences*, *59*(9), 1502–1514, doi:10.1175/1520-0469(2002)059<1502:TMMTCO>2.0.CO;2.

Bowman, K. P., and P. J. Cohen (1997), Interhemispheric Exchange by Seasonal Modulation of the Hadley Circulation, *Journal of the Atmospheric Sciences*, *54*(16), 2045–2059, doi: 10.1175/1520-0469(1997)054<2045:IEBSMO>2.0.CO;2.

Bowman, K. P., and T. Erukhimova (2004), Comparison of Global-Scale Lagrangian Transport Properties of the NCEP Reanalysis and CCM3, *Journal of Climate*, *17*(5), 1135–1146, doi:10.1175/1520-0442(2004)017<1135:COGLTP>2.0.CO;2.

Chen, G., and R. A. Plumb (2014), Effective Isentropic Diffusivity of Tropospheric Transport, *Journal of the Atmospheric Sciences*, *71*(9), 3499–3520, doi:10.1175/JAS-D-13-0333.1.

Dima, I. M., and J. M. Wallace (2003), On the Seasonality of the Hadley Cell, *J. Atmos. Sci.*, *60*, 1522–1527.

Erukhimova, T., and K. P. Bowman (2006), Role of convection in global-scale transport in the troposphere, *J. Geophys. Res.*, *111*(D3), 1–12.

Geller, L., J. Elkins, J. Lobert, A. Clarke, D. Hurst, J. Butler, and R. Myers (1997), Tropospheric SF6: Observed latitudinal distribution and trends, derived emissions and interhemispheric exchange time, *Geophysical research letters*, *24*(6), 675–678, doi: 10.1029/97GL00523.

Gilliland, A. B., and D. E. Hartley (1998), Interhemispheric transport and the role of convective parameterizations, *Journal of Geophysical Research: Atmospheres*, *103*(D17), 22,039–22,045, doi:10.1029/98JD01726.

Haine, T. W. N., H. Zhang, D. W. Waugh, and M. Holzer (2008), On transit-time distributions in unsteady circulation models, *Ocean Modelling*, *21*(1-2), 35–45, doi: 10.1016/j.ocemod.2007.11.004.

Haynes, P., and E. F. Shuckburgh (2000), Effective diffusivity as a diagnostic of atmospheric transport 2. Troposphere and lower stratosphere, *Journal of Geophysical Research*, *105*(D18), 22,795–22,810, doi:10.1029/2000JD900092.

Hazra, A., and V. Krishnamurthy (2015), Space-Time Structure of Diabatic Heating in Monsoon Intraseasonal Oscillation, *Journal of Climate*, *28*(6), 2234–2255, doi:10.1175/JCLI-D-14-00280.1.

Heimann, M., and C. D. Keeling (1986), Meridional eddy diffusion model of the transport of atmospheric carbon dioxide: 1. Seasonal carbon cycle over the tropical Pacific Ocean, *Journal of Geophysical Research*, *91*(D7), 7765, doi:10.1029/JD091iD07p07765.

Held, I. M., and M. J. Suarez (1994), A Proposal for the Intercomparison of the Dynamical Cores of Atmospheric General Circulation Models, *Bulletin of the American Meteorological Society*, *75*(10), 1825–1830, doi:10.1175/1520-0477(1994)075<1825:APFTIO>2.0.CO;2.

Hess, P. G. (2005), A comparison of two paradigms: The relative global roles of moist convective versus nonconvective transport, *J. Geophys. Res.*, *110*(D20), 1–14.

Holzer, M. (1999), Analysis of passive tracer transport as modeled by an atmospheric general circulation model, *Journal of Climate*, *12*(6), 1659–1684, doi:10.1175/1520-0442(1999)012<1659:AOPTTA>2.0.CO;2.

Holzer, M. (2009a), The Path Density of Interhemispheric Surface-to-Surface Transport. Part II: Transport through the Troposphere and Stratosphere Diagnosed from NCEP Data, *Journal of the Atmospheric Sciences*, *66*(8), 2172–2189, doi:10.1175/2009JAS2895.1.

Holzer, M. (2009b), The Path Density of Interhemispheric Surface-to-Surface Transport. Part I: Development of the Diagnostic and Illustration with an Analytic Model, *Journal of the Atmospheric Sciences*, *66*(8), 2159–2171, doi:10.1175/2009JAS2894.1.

Holzer, M., and G. J. Boer (2001), Simulated Changes in Atmospheric Transport Climate, *J. Climate*, *14*(23), 4398–4420.

Holzer, M., and D. W. Waugh (2015), Interhemispheric transit time distributions and path-dependent lifetimes constrained by measurements of SF6, CFCs, and CFC replacements, *Geophysical Research Letters*, *42*(11), 4581–4589, doi:10.1002/2015GL064172.

Levin, I., and V. Hesshaimer (1996), Refining of atmospheric transport model entries by the globally observed passive tracer distributions of 85 krypton and sulfur hexafluoride (SF 6), *Journal of Geophysical Research*, *101*(16), 745–755, doi:10.1029/96JD01058.

Lin, S.-J., W. C. Chao, Y. C. Sud, and G. K. Walker (1994), A Class of the van Leer-type Transport Schemes and Its Application to the Moisture Transport in a General Circulation Model, *Monthly Weather Review*, *122*(7), 1575–1593, doi:10.1175/1520-0493(1994)122<1575:ACOTVL>2.0.CO;2.

Lintner, B. R., A. B. Gilliland, and I. Y. Fung (2004), Mechanisms of convection-induced modulation of passive tracer interhemispheric transport interannual variability, *Journal of Geophysical Research: Atmospheres*, *109*(D13), n/a–n/a, doi:10.1029/2003JD004306.

Lintner, B. R., C. E. Holloway, and J. D. Neelin (2011), Column water vapor statistics and their relationship to deep convection, vertical and horizontal circulation, and moisture structure at Nauru, *Journal of Climate*, *24*(20), 5454–5466, doi:10.1175/JCLI-D-10-05015.1.

Maiss, M., and I. Levin (1994), Global increase of SF 6 observed in the atmosphere, *Geophysical Research Letters*, *21*(7), 569–572, doi:10.1029/94GL00179.

Neelin, J. D., B. R. Lintner, B. Tian, Q. Li, L. Zhang, P. K. Patra, M. T. Chahine, and S. N. Stechmann (2010), Long tails in deep columns of natural and anthropogenic tropospheric tracers, *Geophysical Research Letters*, *37*(5), n/a–n/a, doi:10.1029/2009GL041726.

Orbe, C., M. Holzer, and L. M. L. Polvani (2012), Flux distributions as robust diagnostics of stratosphere-troposphere exchange, *Journal of Geophysical Research*, *117*(D1), D01,302, doi:10.1029/2011JD016455.

634 Orbe, C., D. W. Waugh, P. A. Newman, and S. Steenrod (2016), The Transit-Time Distri-
635   bution from the Northern Hemisphere Midlatitude Surface, *Journal of the Atmospheric*
636   *Sciences*, *73*(10), 3785–3802, doi:10.1175/JAS-D-15-0289.1.

637 Plumb, R. A., and A. Y. Hou (1992), The response of a zonally symmetric atmos-
638   phere to subtropical thermal forcing - Threshold behavior, doi:10.1175/1520-
639   0469(1992)049<1790:TROAZS>2.0.CO;2.

640 Plumb, R. A., and J. D. Mahlman (1987), The Zonally Averaged Transport Characteristics
641   of the GFDL General Circulation/Transport Model, *Journal of the Atmospheric Sciences*,
642   *44*(2), 298–327, doi:10.1175/1520-0469(1987)044<0298:TZATCO>2.0.CO;2.

643 Popovic, J. M., and R. A. Plumb (2001), Eddy Shedding from the Upper-Tropospheric
644   Asian Monsoon Anticyclone, *Journal of the Atmospheric Sciences*, *58*(1), 93–104, doi:
645   10.1175/1520-0469(2001)058<0093:ESFTUT>2.0.CO;2.

646 Shaw, T. A. (2014), On the Role of Planetary-Scale Waves in the Abrupt Seasonal Transition
647   of the Northern Hemisphere General Circulation, *Journal of the Atmospheric Sciences*,
648   *71*(5), 1724–1746, doi:10.1175/JAS-D-13-0137.1.

649 Staudt, A. C., D. J. Jacob, J. A. Logan, D. Bachiochi, T. N. Krishnamurti, and G. W. Sachse
650   (2001), Continental sources, transoceanic transport, and interhemispheric exchange of
651   carbon monoxide over the Pacific, *Journal of Geophysical Research*, *106*(April 1999),
652   32,571–32,589, doi:10.1029/2001JD900078.

653 Waugh, D. W., and T. M. Hall (2002), Age of stratospheric air: Theory, observations, and
654   models, *Rev. Geophys.*, *40*, 1010.

655 Waugh, D. W., R. A. Plumb, and L. M. Polvani (1994), Nonlinear, Barotropic Response to a
656   Localized Topographic Forcing: Formation of a "Tropical Surf Zone" and Its Effect on In-
657   terhemispheric Propagation, doi:10.1175/1520-0469(1994)051<1401:NBRTAL>2.0.CO;2.

658 Waugh, D. W., A. M. Crotwell, E. J. Dlugokencky, G. S. Dutton, J. W. Elkins, B. D. Hall,
659   E. J. Hintsa, D. F. Hurst, S. a. Montzka, D. J. Mondeel, F. L. Moore, J. D. Nance, E. a.
660   Ray, S. D. Steenrod, S. E. Strahan, and C. Sweeney (2013), Tropospheric SF 6 : Age of
661   air from the Northern Hemisphere midlatitude surface, *Journal of Geophysical Research:*
662   *Atmospheres*, *118*(19), 11,429–11,441, doi:10.1002/jgrd.50848.

663 Zhai, J., and W. Boos (2015), Regime Transitions of Cross-Equatorial Hadley Circulations
664   with Zonally Asymmetric Thermal Forcings, *Journal of the Atmospheric Sciences*, *72*,
665   3800–3818, doi:10.1175/JAS-D-15-0025.1.